Check for updates

Batteries & Supercaps

Research Article
doi.org/10.1002/batt.202400335

Chemistry Europe
European Chemical Societies Publishing

www.batteries-supercaps.org

Enhancing the Supercapacitive Behaviour of Cobalt Layered Hydroxides by 3D Structuring and Halide Substitution

Álvaro Seijas-Da Silva[+,[a]] Víctor Oestreicher[+,*[a]] Cristián Huck-Iriart,[b, c] Martín Mizrahi,[d, e] Diego Hunt,[f] Valeria Ferrari,[g, h] and Gonzalo Abellán*[a]

Among the two-dimensional (2D) materials, layered hydroxides (LHs) stand out due to their chemical versatility, allowing the modulation of physicochemical properties on demand. Specifically, LHs based on earth-abundant elements represent promising phases as electrode materials for energy storage and conversion. However, these materials exhibit significant drawbacks, such as low conductivity and in-plane packing that limits electrolyte diffusion. In this work, we explore the synthetic flexibility of α-Co^{II} hydroxides (*Simonkolleite*-like structures) to overcome these limitations. We elucidate the growth mechanism of 3D flower-like α-Co^{II} hydroxyhalides by using in situ SAXS experiments combined with thorough physicochemical, structural, and electrochemical characterization. Furthermore, we compared these findings with the most commonly employed Co-based LHs: β-$Co(OH)_2$ and CoAl layered double hydroxides. While α-Co^{II} LH phases inherently grow as 2D materials, the use of ethanol (EtOH) triggers the formation of 3D arrangements of these layers, which surpass their 2D analogues in capacitive behavior. Additionally, by taking advantage of their anion-dependent bandgap, we demonstrate that substituting halides from chloride to iodide enhances capacitive behavior by more than 40%. This finding confirms the role of halides in modulating the electronic properties of layered hydroxides, as supported by DFT+U calculations. Hence, this work provides fundamental insights into the 3D growth of α-Co^{II} LH and the critical influence of morphology and halide substitution on their electrochemical performance for energy storage applications.

Introduction

Since the first report related with the isolation of graphene,[1] the field of two-dimensional (2D) and layered materials has gained enormous attention by the scientific community.[2,3] In this context, graphene, silicene, germanene, and pnictogens are clear examples of monoelemental 2D systems.[4–8] In addition, multi-elemental 2D layered phases have also been intensively investigated such as boron nitride, transition metal dichalcogenides or oxides, and perovskites, to name a few.[7,9,10]

Among them, layered hydroxides (LHs) stand out as promising and interesting systems of study, mainly due to their unparalleled chemical versatility, low-cost synthetic methods, high surface area, and potential application as electroactive materials.[11–16] Undoubtedly, layered double hydroxides (LDHs), also known as anionic clays, spotlight as one of the most studied members in the LHs family, considering their anion exchange properties, and since 2013 due to their outstanding performance as catalysts for water splitting in basic media.[17–19] The LDH structure consists of positively charged 2D sheets of

[a] Á. Seijas-Da Silva,[+] V. Oestreicher,[+] G. Abellán
Instituto de Ciencia Molecular (ICMol), Universitat de València, Catedrático José Beltrán 2, 46980 Paterna, Valencia, Spain
E-mail: victor.oestreicher@uv.es
Gonzalo.abellan@uv.es

[b] C. Huck-Iriart
Instituto de Tecnologías Emergentes y Ciencias Aplicadas (ITECA), UNSAM-CONICET, Escuela de Ciencia y Tecnología, Laboratorio de Cristalografía Aplicada, Campus Miguelete, 1650 San Martín, Buenos Aires, Argentina

[c] C. Huck-Iriart
ALBA Synchrotron Light Source, Carrer de la Llum 2–26, Cerdanyola del Vallès, 08290 Barcelona, Spain

[d] M. Mizrahi
Instituto de Investigaciones Fisicoquímicas Técnicas y Aplicadas (INIFTA), Departamento de Química, Facultad de Ciencias Exactas, Universidad Nacional de La Plata, CCT La Plata- CONICET. Diagonal 113 y 64, 1900 La Plata, Argentina

[e] M. Mizrahi
Facultad de Ingeniería, Universidad Nacional de La Plata, Calle 1 esq. 47, 1900 La Plata, Argentina

[f] D. Hunt
Departamento de Física de la Materia Condensada, GlyA, CAC-CNEA, Instituto de Nanociencia y Nanotecnología, CNEA-CONICET- San Martin, Buenos Aires, Argentina

[g] V. Ferrari
Instituto Sabato, UNSAM - CNEA, Av. Gral Paz 1499, 1650 San Martín, Buenos Aires, Argentina

[h] V. Ferrari
Instituto de Nanociencia y Nanotecnología, CNEA - CONICET, Departamento de Física de la Materia Condensada, GlyA, CAC - CNEA, Av. Gral Paz 1499, 1650 San Martín, Buenos Aires, Argentina

[+] These authors contributed equally to this work.

Supporting information for this article is available on the WWW under https://doi.org/10.1002/batt.202400335

© 2024 The Authors. Batteries & Supercaps published by Wiley-VCH GmbH. This is an open access article under the terms of the Creative Commons Attribution Non-Commercial NoDerivs License, which permits use and distribution in any medium, provided the original work is properly cited, the use is non-commercial and no modifications or adaptations are made.

© 2024 The Authors. Batteries & Supercaps published by Wiley-VCH GmbH

octahedral M^{II} and M^{III} cations, which can be rationally designed. These layers stack electrostatically with interlayer anions, enabling the preparation of multifunctional LDHs used in catalysis, magnetism, and energy storage, among other fields.[20–23]

However, LDHs own an important limitation when used as electrodes for energy applications: their poor electrical conductivity.[24] To overcome this, the most widely used approach involves obtaining hybrids with conductive or semiconductor materials, such as carbon nanoforms.[25–30] Nevertheless, another less explored option is to exclusively tune the electronic properties of the inorganic layers. For instance, the incorporation of highly valence metal atoms providing new localized states close to the Fermi level, which can be associated with the better performances when LDHs are employed as electrode materials for water splitting and supercapacitors.[31–33] Moreover, the covalent functionalization with donor ligands could be another way to reduce the gap. In this sense, α-Co^{II} hydroxides (or *Simonkolleite*-like structures) are distinguished within the LHs family as they can be considered inherently covalently functionalized structures.[34,35] Unlike LDHs, these materials based on divalent cations exhibit two types of coordination environments: octahedral and tetrahedral.[36] The tetrahedral sites allow the anchoring of different (in)organic anions displaying interesting ligand-property relationships. Indeed, we have recently developed the synthesis through the *epoxide route*[12] of hexagonal particles of α-Co^{II} hydroxyhalides, from fluoride to iodide.[35,37] Interestingly, in these phases the electrical and magnetic properties depend on the nature of the halide: α-Co^{II} hydroxyiodides depict the higher conductivities.[35] These results were understood in terms of an enhancement in the ligand to metal charge transfer (LMCT), as demonstrated by DFT + U simulations.[35,38] Keeping in mind these remarkable features of α-Co^{II} hydroxides, and considering that α-Co^{II} hydroxides can surpass their Co-based LH analogues as electroactive materials for water splitting under alkaline conditions,[34] it would be interesting to study the supercapacitive behaviour of α-Co^{II} hydroxyhalides in comparison with the most common Co-based LHs phases (β-$Co(OH)_2$ and CoAl-LDHs).

Besides conductivity, morphology also plays a key role on electrode materials, even in isolated 2D systems exposing high surface areas. Large 2D flakes tend to spontaneously in-plane align on the electrodes leading to tortuous channels that hinders the electrolyte diffusion.[39] Thus, the 3D arrangement of 2D materials arise as a promising alternative in the field of 2D materials for energy applications.[40–42]

Here, we explored the role of halide substitution (Cl, Br and I) on the supercapacitive electrochemical behavior of 3D flower-like α-Co^{II} hydroxyhalides. Firstly, to understand the growth mechanisms, we performed in situ SAXS experiments during the precipitation process, elucidating the role of EtOH in inducing the aggregation of 2D flakes into 3D flower-like morphologies. Moreover, electrochemical measurements demonstrated that flower-like α-Co^{II} LH surpasses other Co-based LHs, showing a more than 42% enhancement in capacitance (from 564 to 800 F/g at 1 A/g in 6 M KOH) when substituting chloride with iodide.

Results and Discussion

In the search of suitable LHs phases for energy storage, we decided firstly to explore how α-Co^{II} hydroxyhalides (α-Co–X) growth to define specific conditions to drive the occurrence of flower-like morphologies. Taking into account the mild conditions offered by the *epoxide route*, *in situ* experiments can be performed using pH kinetic profiles to identify precipitation steps and thermodynamic stability (solubility).[12,14,35,43,44] These methods can also be applied to more challenging experiments, such as in situ SAXS[45–48]

Therefore, two different synthetic scenarios were studied by *in situ* SAXS experiments conducted at the NCD-SWEET beamline at the ALBA synchrotron. These scenarios involved obtaining single hexagonal particles in aqueous solution,[49] and polycrystalline 3D flower-like morphologies in ethanol-rich solutions ($EtOH:H_2O = 75:25$). SAXS is a well-established technique to analyse the morphology and internal structure of colloidal suspensions.[46] Furthermore, pattern's features provide valuable information useful to unravel the initial nuclei (seeds) symmetry and their development during the synthesis, in diluted systems.[46] Hence, *in situ* experiments allow us to follow, in real time, the particle's evolution without any external perturbation, *e.g.*: quenching.

Figure 1 depicts selected SAXS patterns for α-Co–Cl where the occurrence of 2D seeds can be observed in both cases. These 2D objects, associated with linear slope of −2 in *log vs log* scale centred around $0.04 < q < 0.1$, are observable during the whole precipitation process. It is worth mentioning that under these experimental conditions (sample-detector distance) the lateral size of 2D objects larger than *ca.* 50 nm cannot be estimated. Nonetheless, the dimensionality and average thickness can be accurately determined. Interestingly, while in the experiments driven in aqueous solution the thickness increases from *ca.* 5.5–12.9 nm, those ones taking place in ethanol-rich mixtures are slightly thinner (from 5.0–8.4 nm). TEM images (Figure 1 - inset) depict the occurrence of micrometric hexagonal particles and flower-like morphologies. Based on these results, the formation of flower-like structures can be attributed to factors including colloidal stability, viscosity, and the dielectric constant of the solvents. In aqueous solutions, layered hydroxides typically form hexagonal shapes that stack easily and increase in thickness. This is facilitated by water's higher dielectric constant, which reduces electrostatic repulsion between layers, allowing for tighter packing. In contrast, ethanol's lower dielectric constant promotes the aggregation and flocculation of small 2D crystalline seeds during the precipitation process, inhibiting growth in the perpendicular direction and resulting in thinner crystals. Additionally, the increased viscosity in ethanol-rich environments, similar to ethylene glycol-water mixtures, exacerbates the Ostwald ripening process.[21] This leads to smoother aggregate surfaces and their eventual splitting into smaller, curved nanosheets. These characteristics unique to ethanol-rich environments foster the distinct 3D flower-like structures, contrasting with those formed in aqueous media. It is worth mentioning that SAXS patterns of the flower-like particles are consistent with non-close range-

© 2024 The Authors. Batteries & Supercaps published by Wiley-VCH GmbH

25666223, 2024, 11, Downloaded from https://chemistry-europe.onlinelibrary.wiley.com/doi/10.1002/batt.202400335 by University of Ulsan, Wiley Online Library on [11/11/2025]. See the Terms and Conditions (https://onlinelibrary.wiley.com/terms-and-conditions) on Wiley Online Library for rules of use; OA articles are governed by the applicable Creative Commons License

Research Article
doi.org/10.1002/batt.202400335
Chemistry Europe
European Chemical Societies Publishing

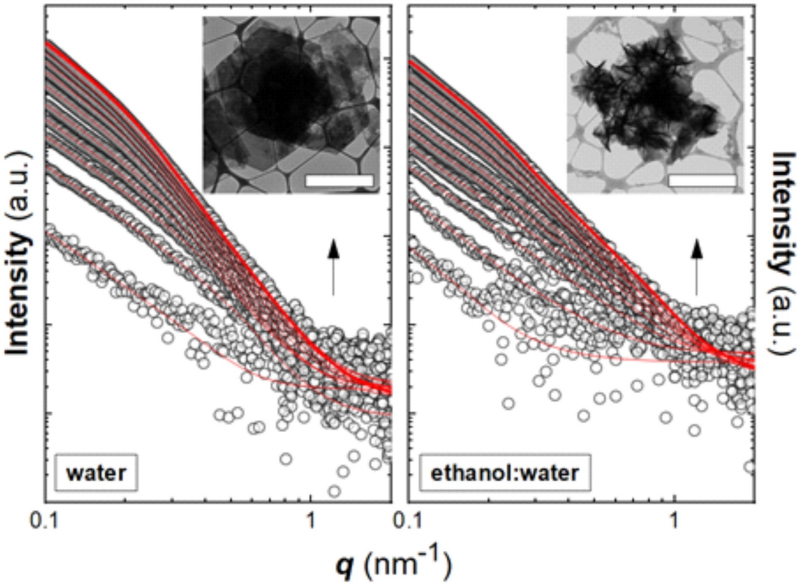

Figure 1. In situ of SAXS patterns (dots) and fittings (red lines) recorded during precipitation of α-Co^{II} hydroxychlorides in aqueous (left) and ethanol-rich solution. The slopes of −2 in the range of $q = 0.4$–1.0 confirm the presence of 2D objects during the whole precipitation process. Arrows indicate the evolution. Insets: TEM images of the obtained phases. Scale bar: 1 μm.

interacting 2D objects even after extended reaction times (indicated by a slope of −2 in *log vs log* scale). Therefore, we can conclude the 2D nature of the layers composing the 3D flower-like structures. Once demonstrated that EtOH can trigger the occurrence of flower-like morphologies for α-Co–Cl, even at low ionic strength,[49] we decided to extend this tool to other α-Co^{II} hydroxyhalides, namely α-Co^{II} hydroxybromides (α-Co–Br) and α-Co^{II} hydroxyiodides (α-Co–I). For that, keeping unaltered the EtOH:H_2O ratio in the experiments (75:25), Gly concentrations were adjusted for bromide and iodide considering their nucleophilic behaviour (further details in Experimental Section).[35] In this sense, the precipitation has been driven to simultaneously guarantee the onset of precipitation (see Figure S1).[35] Figure 2 depicts the TEM and SEM images where the occurrence of flower-like morphologies is observed for all the α-Co–X samples, in contrast to those previously synthesized in pure aqueous media.[35,49,50] Figure S2 presents the *in situ* SAXS patterns where it is possible to observe an analogous growth pathway for all the α-Co–X. In overall, the growth process of the α-Co^{II} hydroxyhalides exhibiting a flower-like structure has been understood as changes in colloidal stability that trigger the coalescence of primary seeds, which develop into polycrystalline systems.

Figure 3A depicts the PXRD patterns recorded for the solid green-blueish samples. In all the cases the typical reflection pattern for α-Co^{II} hydroxyhalides is observed.[35,36,51] While the first main reflections, {003} and {006}, correspond to the basal space distances ($d_{BS} = \frac{1}{2}[d_{003} + d_{006}]$), the intralayer distance can be extracted from the {110} reflection located *ca.* 58°. In the case of the basal space distance's reflection, a clear shift to lower *2-theta* values is observed from α-Co–Cl to α-Co–I LHs, confirming the incorporation of the desired halide: the higher the halide the larger the d_{BS}, as expected.[35] Additionally, to further confirm the occurrence of α-Co^{II} hydroxyhalides, UV-Vis diffuse reflectance spectroscopy was employed to unequivocally confirm the presence of both environments, $Co^{II}(O_h)$ and $Co^{II}(T_d)$, and the coordinated anions.[52,53] Typically, while $Co^{II}(O_h)$ cations are assigned to a broad, low intensity signal

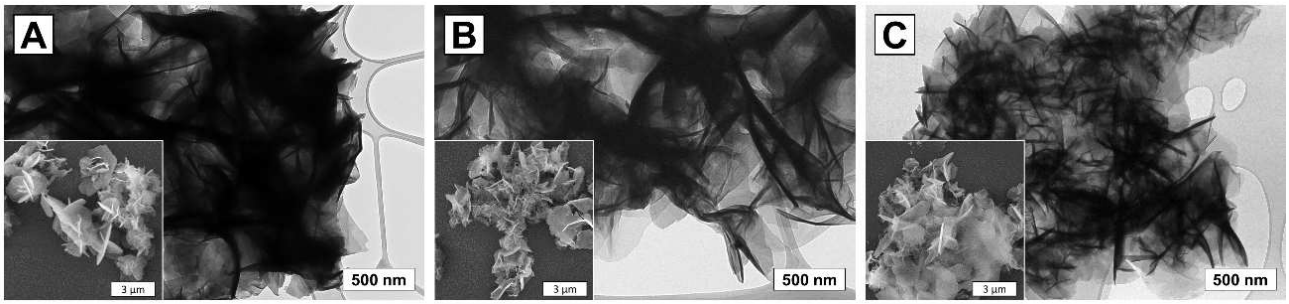

Figure 2. TEM and SEM (inset) images for α-Co^{II} hydroxyhalides samples synthetized by employing the *epoxide route* and solvent mixtures EtOH:H_2O = 75:25. (A) α-Co–Cl, (B) α-Co–Br and (C) α-Co–I.

© 2024 The Authors. Batteries & Supercaps published by Wiley-VCH GmbH

25666223, 2024, 11, Downloaded from https://chemistry-europe.onlinelibrary.wiley.com/doi/10.1002/batt.202400335 by University of Ulsan, Wiley Online Library on [11/11/2025]. See the Terms and Conditions (https://onlinelibrary.wiley.com/terms-and-conditions) on Wiley Online Library for rules of use; OA articles are governed by the applicable Creative Commons License

Research Article
doi.org/10.1002/batt.202400335

Chemistry Europe
European Chemical Societies Publishing

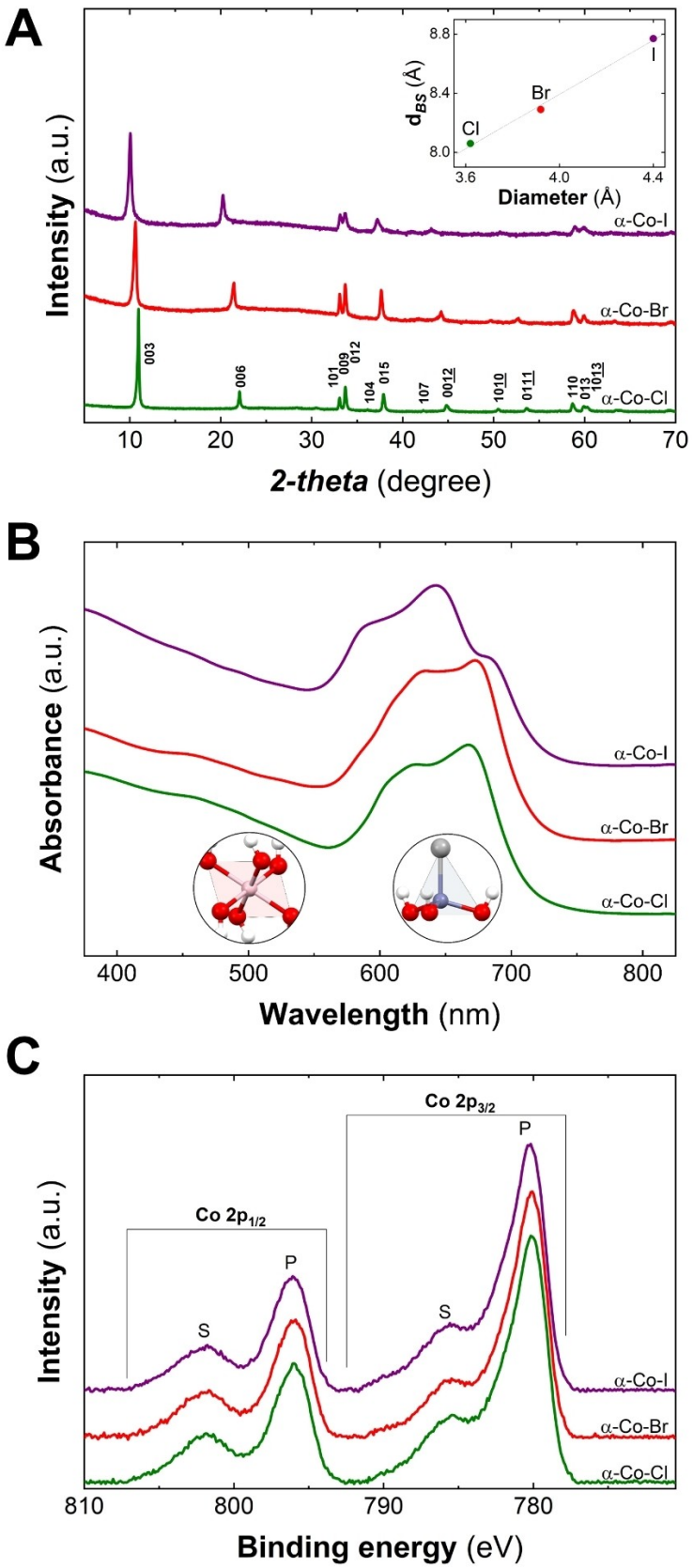

Figure 3. PXRD patters (inset: correlation between the anionic diameter and the basal space distance) (A), UV-Vis diffuse reflectance spectra, highlighting O_h and T_d region with the structures. (B), and high resolution XPS for Co 2p in the range 810–775 eV, with its fitting denoting the signals attributed to peaks and satellites form Co $2p^{3/2}$ and $2p^{1/2}$ (C), for the family α-Co–X containing chloride (α-Co–Cl), bromide (α-Co–Br) and iodide (α-Co–I).

© 2024 The Authors. Batteries & Supercaps published by Wiley-VCH GmbH

25666223, 2024, 11, Downloaded from https://chemistry-europe.onlinelibrary.wiley.com/doi/10.1002/batt.202400335 by University of Ulsan, Wiley Online Library on [11/11/2025]. See the Terms and Conditions (https://onlinelibrary.wiley.com/terms-and-conditions) on Wiley Online Library for rules of use; OA articles are governed by the applicable Creative Commons License

Research Article
doi.org/10.1002/batt.202400335
Chemistry Europe
European Chemical Societies Publishing

around 500 nm, the strong bands located in the range between 550 and 700 nm are ascribable to $Co^{II}(T_d)$ centres.[36,54] In this range $Co^{II}(T_d)$ centres exhibit three distinct energetic transitions, which are crucial in determining their spectroscopic signatures.[55] Interestingly, while samples containing chloride and bromide are associated with a twin-peaks like band, iodide one depicts a three-peak one. This difference in the spectra can be attributed to the iodide's stronger ligand field and more pronounced spin-orbit coupling effects. Iodide, with its larger atomic size and greater mass, interacts more intensively with the d-orbitals of cobalt. This enhanced interaction leads to a greater splitting of these orbitals, as clearly demonstrated by the three distinct peaks in the UV-Vis spectra, in contrast to the twin-peak pattern observed in the chloride and bromide samples.[55] At the same time, the maximum position strongly depends on the nature of the halide, being a suitable fingerprint to identify the coordinated anions, either inorganic or organic, in these LHs (see Table S1).[35,53,56] XPS confirms the occurrence of superficial Co^{II} in all the cases by the presence of the main peaks at 780.3 ± 0.1 eV ($2p_{3/2}$) and 796.1 ± 0.1 eV ($2p_{1/2}$), and their satellites at 785.4 ± 0.1 eV and 801.9 ± 0.1 eV, respectively. An extended analysis of the deconvoluted X-ray photoelectron spectroscopy (XPS) spectra is presented in the Supplementary Information (Figure S3). This detailed examination confirms that the oxidation state of cobalt consistently remains at +2 across all samples. The peak fitting protocol, involving the assignment of two main peaks and two satellite peaks for the $2p_{3/2}$ region, adheres to the methodology detailed by Biesinger et al. in their comprehensive analysis of XPS for transition metals.[57] Furthermore, the analysis reveals subtle shifts to higher binding energies for the peaks, as the anion is altered from chloride to iodide. These shifts underscore the influence of anionic modification on the electronic environment surrounding the cobalt centers, affirming the sensitivity of cobalt's electronic structure to halide ion variations.

Additionally, in order to define the halide:cobalt ratio, EDS and XPS were performed assessing information from both bulk and surface (see Figure S3). Both techniques indicate a higher amount of halide in case of the smaller one, hence the presence of $Co^{II}(T_d)$ can be modulated by choosing the halide's size. Table S2 compiles the chemical composition estimated by EDS, XPS, and TGA (see Figure S4).

Further electronic and structural information of the samples was obtained by X-Ray Absorption Spectroscopy (XAS), in the region near to the edge (XANES), and in the extended region (EXAFS) of the spectrum. Figure 4A depicts the Co K-edge XANES absorption spectra (measured by transmission) of the set of studied samples, where the occurrence of Co^{II} (by means of pre peak, absorption edge and maximum) can be confirmed for all the hydroxyhalide structures.[52] Figure 4B shows the Fourier Transform (FT) of the EXAFS oscillations at the Co K-edge. There are two major contributions between 1 and 3 Å, these representing the average distances (without phase correction) to the first and second coordination shells around the Co atoms, respectively. Looking the first peak, we can notice that its FWHM is wider than usual for all cases. This contribution contemplates the presence of two Co–O distances very similar

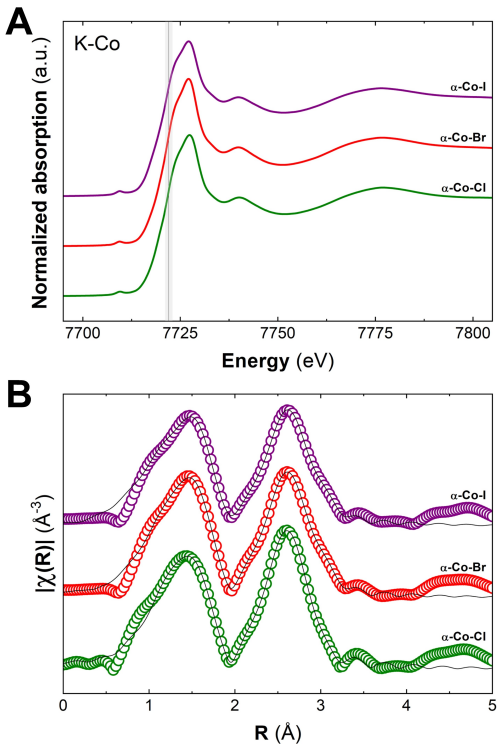

Figure 4. Normalized XANES spectra at the Co K-edge. The black line depicts the expected position for cobalt atoms exhibiting oxidation state +2 (A). Fourier transform of the extracted κ^2-weighted EXAFS oscillations, for the measured samples-circles-and their corresponding fittings-black line. In all of the cases, the XAS spectra are represented without phase correction.

to each other. Furthermore, we can notice that this first peak moves towards greater distances in the α-Co–Br and α-Co–I samples, compared to its position for the α-Co–Cl, while the second peak remains at the same position for all of them. The latter is also in agreement with the existence of $Co^{II}(O_h)$ and $Co^{II}(T_d)$ environments in the samples, where the Co–Co distances are practically the same.[34,36,52]

To obtain the structural parameters (coordination numbers (N), interatomic distances (R) and structural disorder (σ^2)) of the formed phases, EXAFS fits were performed. According to the characteristic of the first peak mentioned above, it was decided to use a model with two Co–O coordination spheres, with similar distances from each other, indicative of some Co atoms in O_h environments, and others in T_d sites. In addition, a third coordination sphere of Co atoms is included, which considers Co–Co distances in both environments. The results of the fits are shown in Figure 4B (solid black lines) and in Table S3. The quality of the fits is very good in all cases, showing that the models proposed for each sample meet the minimum requirements for the reproduction of radial distributions. The Co–O distances obtained for samples were of the order of 1.87 Å and 2.13 Å, which are in very good agreement with the presence of $Co^{II}(O_h)$ and $Co^{II}(T_d)$ environments, respectively. The average coordination number obtained for the shell corresponding to the T_d environment is higher in the α-Co–Cl sample, which indicates a higher fraction of $Co^{II}(T_d)$ moieties, in agreement with XPS and EDS data.

© 2024 The Authors. Batteries & Supercaps published by Wiley-VCH GmbH

25666223, 2024, 11, Downloaded from https://chemistry-europe.onlinelibrary.wiley.com/doi/10.1002/batt.202400335 by University of Ulsan, Wiley Online Library on [11/11/2025]. See the Terms and Conditions (https://onlinelibrary.wiley.com/terms-and-conditions) on Wiley Online Library for rules of use; OA articles are governed by the applicable Creative Commons License

Research Article
doi.org/10.1002/batt.202400335
Chemistry Europe
European Chemical Societies Publishing

Furthermore, we performed theoretical simulations to deepen our understanding of the conducting properties exhibited by α-Co^{II} hydroxyhalides. The projected and total density of states for three representative supercells [$Co_n^{Oh}Co_2^{Td}(OH)_{2n+2}X_2$] (n = 3, n = 8 and n = 15) for α-Co^{II} hydroxyhalide are depicted in Figure S5, where the role of the halide and Co(Td) concentration (from 13–40 %) can be clearly observed. As the number of Co(Td) sites increases, the electronic states of halide atoms play a more significant role near the valence bands due to the ligand-metal charge transfer. Moreover, the primary contribution to the conduction bands comes from the electronic states of both types of cobalt cations, in tetrahedral and octahedral environments. Nevertheless, as the concentration of octahedral sites rises, the electronic states of O atoms and octahedral cobalt cations display a substantial impact in the vicinity of the Fermi level, promoting the closing of the energy gap, and thus, increasing the conducting properties of these materials.

Regarding electrochemistry, it is worth mentioning that the capacitive behaviour of Co^{II}-based LHs (α-, β-, LDH, etc.) arise from faradaic processes taking place in the Co cations, *i.e.* redox reactions. In fact, for the simplest Co-based LHs, the β structure, Faraday's laws suggest a theoretical specific capacitance of *ca.* 2000 F/g. However, this ideal value remains unachievable mainly by limitations in the faradaic processes such as the inherent lack of conductivity of the LHs or the limited electrolyte diffusion, to name a few.[58] In this sense, α-Co^{II} hydroxyhalides spotlight due to its intrinsic lower bandgap and expanded structure,[35,38] with marked effect on the electrocatalytic behaviour as we have recently demonstrated.[34] Therefore, we decided to study the electrochemical performance (redox behaviour) of α-Co^{II} hydroxychloride by cyclic voltammetry curves (CV) in comparison with the typically employed Co-based LHs, β-$Co(OH)_2$ and CoAl-LDH exhibiting hexagonal morphology (Figure 5). The CV measurements recorded at 5 mV/s indicate a unique oxidation peak around 320 mV vs. Ag/AgCl for β-$Co(OH)_2$ and CoAl-LDH, as reported elsewhere.[59,60] However, α-Co–Cl sample exhibit two oxidation peaks. To exclude a possible effect of the substrate (current collector),[61] cyclic voltammetry measurements were conducted on carbon paper using 6 M KOH. Figure S6 depicts an analogous behavior, highlighting the presence of two redox peaks for Co centers in the case of the α-Co sample. These results alert about different reactivity of Co, and therefore distinct cationic environments from the electrochemical point of view. Therefore, these results demonstrate that in α-Co–Cl, some cobalt atoms exhibit a very similar reactivity to those in β-$Co(OH)_2$ and CoAl-LDH, while others are more susceptible to oxidation (faradic process occurring at lower potential values), illustrating the impact of covalently modified $Co^{II}(T_d)$ with anions on the electronic properties and, in consequence, the redox properties.[34,38]

The area below the CV curves is indicative of the capacitive behaviour of the electrochemical phases. The larger the area, the higher the capacitance. Therefore, α-Co–Cl samples present a better electrochemical response in terms of capacitance values in comparison with the other Co-based LHs. Figure 5 presents the specific capacitance calculated from the discharge curves for all the Co-based LHs phases (discharge curves are available in Figure S7). From the specific capacitance values, we can conclude the important role that plays the d_{BS}: expanded structures depict better values (> 5-fold). Specifically, 80, 468 and 566 F/g are obtained at 1 A/g for β-Co(OH)2, CoAl-LDH and α-Co–Cl, respectively. These results can be interpreted based on the improved accessibility of the electrolyte into the material, as it was demonstrated for LDHs phases in energy storage[22] and conversion applications.[62] Nevertheless, despite CoAl-LDH and α-Co–Cl phases exhibit an almost identical d_{BS} values (7.5 and 8.1 Å, respectively), they behave differently as a function of the current density. While α-Co–Cl presents better performance at lower values, CoAl-LDH distinguish at higher ones. Since diffusion has a major role at higher current densities, these results should be related with the higher porosity of Al^{III}-based

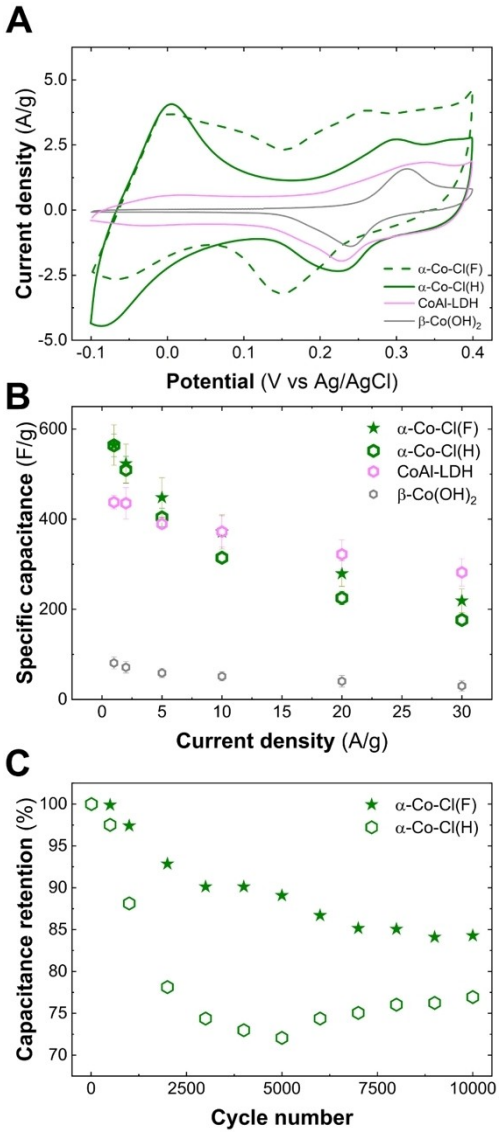

Figure 5. Cyclic voltammetry recorded at 5 mV/s (A) and specific capacitance (B) for Co-based LHs. In the case of α-Co–Cl samples with different morphologies, hexagonal (H) and flower-like (F), stability test at 20 A/g expressed as capacitance retention is presented (C).

© 2024 The Authors. Batteries & Supercaps published by Wiley-VCH GmbH

25666223, 2024, 11, Downloaded from https://chemistry-europe.onlinelibrary.wiley.com/doi/10.1002/batt.202400335 by University of Ulsan, Wiley Online Library on [11/11/2025]. See the Terms and Conditions (https://onlinelibrary.wiley.com/terms-and-conditions) on Wiley Online Library for rules of use; OA articles are governed by the applicable Creative Commons License

Research Article
doi.org/10.1002/batt.202400335
Chemistry Europe
European Chemical Societies Publishing

LDHs which takes place through Aluminium dissolution under alkaline conditions.[22,63,64]

Along this front, the morphology can also play an important role in the improvement of the diffusion.[65–67] For this, α-Co^{II} hydroxychlorides in the form of single hexagonal crystals (α-Co–Cl(H)) and flower-like morphologies (α-Co–Cl(F)), were evaluated. While both behave identically at low current densities, flower-like structure depicts a better performance of *ca.* 25% (>50 F/g) at 30 A/g. Therefore, these results can be correlated to a better diffusion of the electrolyte by an increment in the surface area attributed to this morphology. This point has been corroborated by CO_2 sorption isotherms (see Figure S8).[65] Even more, by analysing the cycling stability (a fundamental factor for its application in real supercapacitors), it can be observed that α-Co–Cl(F) sample remains an 85% of the initial capacitance, up to 10% more than α-Co–Cl(H), in agreement with previous studies on LDH phases (Figure 5).[65,68]

Once demonstrated that α-Co^{II} hydroxides exhibiting 3D flower-like morphology are promising materials for energy storage, we decided to study the role of the halide-substitution on these phases. Figure 6 illustrates the comparative cyclic voltammetry (CV) curves at 5 mV/s for α-Co–X LHs. In all cases, two redox zones are detected, attributed to cobalt species with different redox reactivities: one in the range of 250–300 mV, and the other at much lower potentials. Interestingly, these redox peaks depict a clear shift to lower values (*ca.* 30 mV) depending on the halide, suggesting changes in the electronic properties. Additionally, in the case of α-Co–I the separation of oxidation and reduction peaks become closer, indicative of an enhancement of the reversibility in the redox process. In this line, the specific capacitance values for the α-Co–X LHs, calculated from discharge curves (Figures 5B and S9), increase from α-Co–Cl to α-Co–I. Remarkably, while the halide substitution triggers an enhancement in the specific capacitance of more than 40% at low current densities (from 564–800 F/g), at 30 A/g the increment arises up to 70% (from 219–370 F/g). Furthermore, considering the theoretical capacitance of each phase (see Table S2) an increment in the percentage of electroactive Co centres by halide replacement near to 20% is observed (see Figure 5). In overall, these results reinforce our hypothesis about the role of the halide substitution in controlling the electronic properties of LHs, enlightening the connection between the whole electrochemical performance and the electrical conductivity, as suggested by DFT+U calculations.[35] Last but not least, it is worth mentioning that our α-Co–I sample competes favourably with the best reported pure Co-based LHs, exhibiting nanocone morphology and d_{BS} of 24 Å (see Table S3).[69–72]

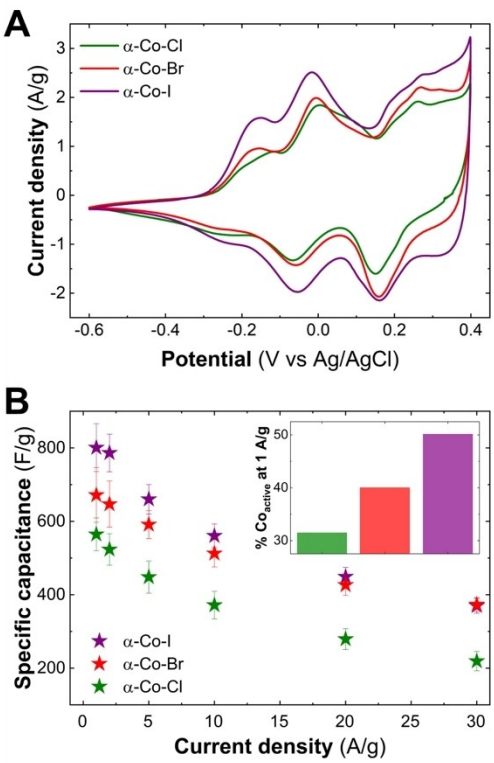

Figure 6. Cyclic voltammetry recorded at 5 mV/s (A) and specific capacitance (B) for α-Co–X LHs exhibiting flower-like morphology. The inset depicts the electroactive Co percentage at 1 A/g.

To shed light on the electrochemical processes occurring on these LHs, a kinetic analysis was performed. We aim to analyse the diffusion and capacitive contributions separately.[73] For that, α-Co–X LHs were characterized by CV curves from −0.6–0.4 V at different scan rates from 100–5 mV/s^1 (see Figure S10). In this sense, the dependence between current density (i_P) and scan rate (v) can be modelled by the Equation (1):[74,75]

$$i_P = a \cdot v^b \tag{1}$$

where a is an adjustable parameter and b strongly depends on the relative contribution between the diffusion and the capacitive processes. Indeed, b value counts whether the current density is strictly dominated by diffusion ($b = 0.5$) or capacitive ($b = 1$) processes. By linearizing of Equation (1), a and b values can be easily obtained (see Equation 2):

$$log i_P \cdot = log a + b log v \tag{2}$$

Figure 7 depicts the electro-kinetic study for the redox behaviour taking place in the α-Co–X samples, where b values are determined from the anodic peaks in both regions, separately (Figure 7A and B). While in the case of the region from 0.1–0.4 V a pure capacitive behaviour can be concluded ($b \approx 1$); in the region from −0.6–0.1 V, the analysis suggests a redox nature controlled by both capacitive and diffusion processes ($0.5 < b_{anodic} < 1.0$), in all the cases. Therefore, to elucidate their contributions at low voltage redox process, the current density response at a given potential is analysed as the combination of capacitive effects ($k_1 v$) and diffusion-controlled reactions ($k_2 v^{1/2}$) according to Equation (3):[76]

$$i(V) = k_1 v + k_2 v^{1/2} \tag{3}$$

where k_1 and k_2 constants count the current's fraction of each process, respectively. Figure 7C depicts the relative enhancement of the constants (k_1 and k_2) in comparison to the

© 2024 The Authors. Batteries & Supercaps published by Wiley-VCH GmbH

25666223, 2024, 11, Downloaded from https://chemistry-europe.onlinelibrary.wiley.com/doi/10.1002/batt.202400335 by University of Ulsan, Wiley Online Library on [11/11/2025]. See the Terms and Conditions (https://onlinelibrary.wiley.com/terms-and-conditions) on Wiley Online Library for rules of use; OA articles are governed by the applicable Creative Commons License

Research Article
doi.org/10.1002/batt.202400335
Chemistry Europe
European Chemical Societies Publishing

obtained ones for α-Co–Cl sample. Interestingly, both constants increase by the halide replacement. Nevertheless, the effect over k_1 (capacitive process) is much higher in comparison with k_2 (diffusion-controlled process), *ca.* 135 and 40%, respectively. Furthermore, to evidence the proportion of both processes on the charge-discharge reaction, the capacitive ones are denoted as the painted area below the curves (Figure 7D–F). From α-Co–Cl to α-Co–I sample a clear increment in the capacitive currents is observed, empathising a higher capacitive performance. Additionally, other scan rates were also analysed, where it is possible to observe that diffusion contributions become more relevant at lower scan rates, as expected (see Figure S10). Thus, considering that redox reactions taking place at the interlayer space require the diffusion of the electrolyte,[77] our results indicate that while less reactive Co species are not limited by diffusion, the reactivity of more active Co species strongly depends on the nature of the halide, which controls the electronic properties (see Figure S11).

Finally, electrochemical impedance spectroscopy (EIS) measurements were carried out by applying an alternating-current (AC) amplitude of 10 mV in the frequency range from 10^{-2}–10^{4} Hz at the open circuit potential (Figure 7G). The data is fitted by employing an equivalent circuit composed of two resistances (Figure 7G-inset): the ohmic (R_S), calculated as the intersection point on the real axis at high-frequencies; and the charge-transfer (R_{CT}) one, also called Faraday resistance, obtained from the semicircle fittings (Figure 7H). Furthermore, diffusion and pseudocapacitance processes are represented by a Warburg (***W***) and a constant phase element (***CPE***), at low-frequencies. While R_S values depend mostly on ionic resistance of the electrolyte, intrinsic resistance of contact, resistance at the active material/current collector interface, to name a few;[78] R_{CT} ones are governed mainly by the conductivity of the materials.[79–81] Figure 7I compiles the obtained R_{CT} values for the α-Co–X family, where the α-Co–I sample depicts an almost 40% lower values in comparison with α-Co–Cl one. The R_{CT} diminution as a function of the halide evidence a fast electron transport mainly due to the increment in the conductivity,[82] as we reported for water splitting experiments,[34] and in perfect agreement with DFT + U calculation[38] and conductivity measurements.[35] In the low-frequency region, α-Co–I LHs exhibit a notably steeper slope, indicating enhanced capacitive behaviour and aligning with the specific capacitance derived from charge/discharge cycles. Building on this understanding of the electrochemical processes, we can affirm that halide substitution significantly enhances capacitive behaviour. This

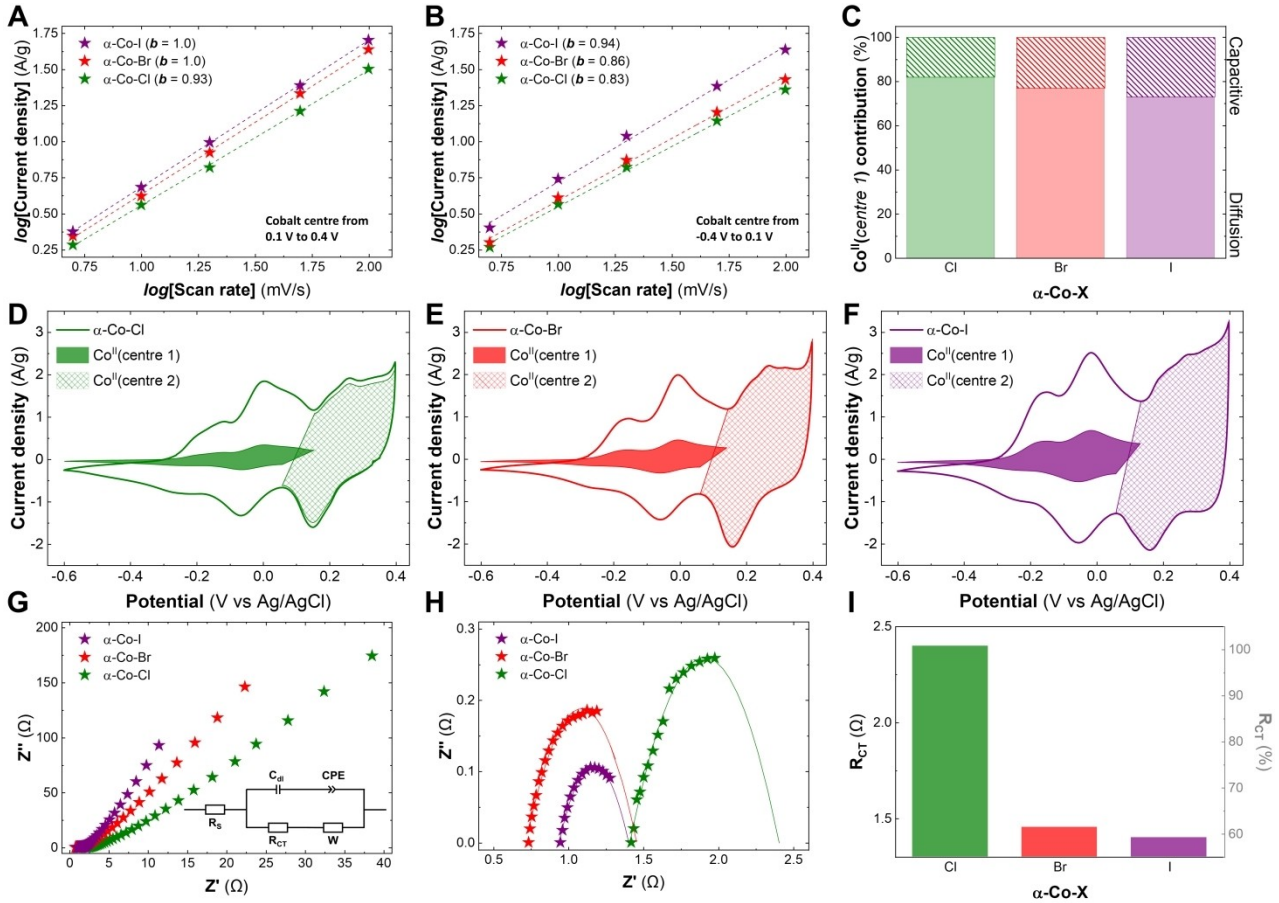

Figure 7. The calculated b values by means of a linear fitting of **log***i_P* on **log***v* in *Co centre form* 0.1 *to* 0.4 *V* (A) and *Co centre form* − 0.4 *to* 0.1 *V* (B) regions from CV data, calculated diffusion and capacitive constants of α-Co–X family in the *Co centre form* − 0.4 *to* 0.1 *V*region (C), Capacitive contribution to the total CV current at 5 mV/s for α-Co–Cl (D), α-Co–Br (E) and α-Co–I (F), electrochemical impedance spectroscopy (EIS) data and equivalent circuit (G), semicircle adjust of high frequency region of EIS data (H) and calculated R_{CT} (I) for α-Co–X family.

© 2024 The Authors. Batteries & Supercaps published by Wiley-VCH GmbH

25666223, 2024, 11, Downloaded from https://chemistry-europe.onlinelibrary.wiley.com/doi/10.1002/batt.202400335 by University of Ulsan, Wiley Online Library on [11/11/2025]. See the Terms and Conditions (https://onlinelibrary.wiley.com/terms-and-conditions) on Wiley Online Library for rules of use; OA articles are governed by the applicable Creative Commons License

enhancement is primarily due to the influence of anions on the electronic and transport properties of layered hydroxides, which leads to an increased specific capacity.

To summarize, the rational design of α-Co^{II} layered hydroxides with donor-coordinated anions induces alterations in the redox behavior of the Co-based LHs, facilitating the production of highly electroactive materials.

Conclusions

In this work we investigated the synthesis of flower-like α-Co^{II} hydroxyhalides and their electrochemical behavior as electrode materials for energy storage. Initially, we elucidated the growth mechanism through in situ SAXS experiments conducted during the precipitation process. It was observed that α-Co^{II} LHs inherently grow as 2D materials, and the addition of EtOH induces the aggregation of native seeds, thereby triggering the formation of flower-like structures. Interestingly, the nature of the 2D LHs persists within these 3D flower-like structures. In terms of electrochemical behavior, the 3D α-Co^{II} LHs containing chloride exhibit superior capacitive performance compared to both hexagonal α-Co^{II} LHs and commonly used Co-based LHs. Furthermore, the halide substitution of chloride by iodide triggers an enhancement in the specific capacitance higher than 40%. This work positions flower-like α-Co^{II} hydroxides as excellent electrode materials for energy storage applications, with potential conductivity improvements achievable through anion substitution.

Experimental

Chemicals

Cobalt chloride hexahydrate ($CoCl_2.6H_2O$), cobalt nitrate hexahydrate ($Co(NO_3)_2.6H_2O$), aluminium chloride hexahydrate ($AlCl_3.6H_2O$), sodium chloride (NaCl), sodium bromide (NaBr), sodium iodide (NaI), urea, hexamethylenetetramine (HMT), glycidol (Gly), acetylene black, and polytetrafluoroethylene (PTFE) were purchased from Sigma-Aldrich. Potassium hydroxide KOH (99.99%) and ethanol absolute (EtOH) were purchased from Panreac. All chemicals were used as received. Milli-Q water was obtained from a Millipore Milli-Q equipment.

Synthesis of α-Co^{II} Hydroxyhalides

The solid phases were obtained employing the *epoxide route*. This homogeneous alkalinisation process consists in the nucleophilic attack of an anion, typically halides, over the electrophilic carbon atom belonging to the epoxide ring. Therefore, the reaction results in the ring-opening and halohydrine formation, with a net alkali generation. Typically, the alkalinisation rate depends on the chemical identity and concentration of both, the nucleophile and the epoxide: $\boldsymbol{v}_{[OH^-]} = \boldsymbol{k}_{X^-}[\boldsymbol{X}^-][\boldsymbol{Gly}]$. In the case of the halides, the kinetic constant can be strongly enhanced by choosing the anion: ($\boldsymbol{k}_{Cl^-} : \boldsymbol{k}_{Br^-} : \boldsymbol{k}_{I^-} = 25 : 5 : 1$). Hence, the concentration must be controlled to ensure analogous kinetics profiles. Typically, precipitations were driven by ageing solutions for 24–48 h at room temperature. The solids were obtained by filtration, washed three times with H_2O:EtOH mixtures and finally with EtOH. Finally, samples were dried at room temperature and kept in desiccators for further characterization.

α-Co^{II} Hydroxychloride Single Crystal Hexagons

The synthesis was performed by aging 48 h at room temperature aqueous solutions containing: [$CoCl_2$] = 10 mM, [NaCl] = 30 mM and [Gly] = 400 mM.

α-Co^{II} Hydroxychloride Flower-Like Morphology

The synthesis was performed by aging 24 h at room temperature ethanol:water (75:25) solutions containing: [$CoCl_2$] = 10 mM, [NaCl] = 30 mM and [Gly] = 2000 mM.

α-Co^{II} Hydroxybromide Flower-Like Morphology

The synthesis was performed by aging 24 h at room temperature ethanol:water (75:25) solutions containing: [$Co(NO_3)_2$] = 10 mM, [NaBr] = 50 mM and [Gly] = 400 mM.

α-Co^{II} Hydroxyiodide Flower-Like Morphology

The synthesis was performed by aging 24 h at room temperature ethanol:water (75:25) solutions containing: [$Co(NO_3)_2$] = 10 mM, [NaI] = 50 mM and [Gly] = 80 mM.

Hydrothermal Synthesis of β-Co^{II} Hydroxide Single Crystal Hexagons

The obtaining of β-Co^{II} hydroxide phase under hydrothermal conditions was carried out by hydrolysis of hexamethylenetetramine (HMT) in 100 mL H_2O:EtOH mixtures (9:1) at 90 °C for 1 h, under N_2 atmosphere. Single crystalline hexagons were synthesized by employing initial concentrations of: [$CoCl_2$] = 5 mM and [HMT] = 60 mM.[50]

Hydrothermal Synthesis of Co^{II}Al^{III} Layered Double Hydroxide Single-Crystal Hexagons

The obtaining of CoAl layered double hydroxide (LDH, CoAl(HT)) phase was carried out by hydrolysis of urea in aqueous solution at *ca.* 97 °C for 48 hs, under N_2 atmosphere, by employing initial concentrations of: [$CoCl_2$] = 10 mM, [$AlCl_3$] = 5 mM, [urea] = 35 mM.[83]

Chemical and Structural Characterization

Powder X-ray powder diffraction (PXRD) patterns were obtained employing a PANalytical Empyrean X-ray platform with a capillary platform and copper radiation (Cu Kα = 1.541 78 Å) in the *2-theta* range 2–70°. UV/Vis absorption spectra of the solid samples were recorded in a reflectance mode employing a Jasco V-670 spectrometer. Field Emission Scanning Electron Microscopy (FESEM) and Energy Dispersive X-ray (EDS) Spectroscopy studies were performed on a Hitachi S-4800 microscope at an accelerating voltage of 20 kV. Transmission electron microscopy (TEM): TEM studies were performed on a JEM-1010 operating at 80 kV. Samples were prepared by dropping suspensions on lacey Formvar/carbon copper grids (300 mesh). X-ray Photoelectron Spectroscopy (XPS) was performed ex situ at the X-ray Spectroscopy Service at the Universidad de Alicante using a K_α X-ray photoelectron spectrom-

© 2024 The Authors. Batteries & Supercaps published by Wiley-VCH GmbH

25666223, 2024, 11, Downloaded from https://chemistry-europe.onlinelibrary.wiley.com/doi/10.1002/batt.202400335 by University of Ulsan, Wiley Online Library on [11/11/2025]. See the Terms and Conditions (https://onlinelibrary.wiley.com/terms-and-conditions) on Wiley Online Library for rules of use; OA articles are governed by the applicable Creative Commons License

eter system (Thermo Scientific). All spectra were collected using Al Kα radiation (1486.6 eV), monochromatized by a twin crystal monochromator, yielding a focused X-ray spot (elliptical in shape with a major axis length of 400 μm) at 3 mA C and 12 kV. The alpha hemispherical analyser was operated in the constant energy mode with survey scan pass energies of 200 eV to measure the whole energy band and 50 eV in a narrow scan to selectively measure the particular elements. XPS data were analysed with Advantage software. Carbon dioxide adsorption/desorption isotherms at 298 K were collected in an AUTOSORB-6 apparatus. Samples were previously degassed at 423 K for 12 h under vacuum with an AUTOSORB DEGASSER. Thermogravimetric analysis (TGA) of all samples was performed on a Mettler Toledo TGA/DSC2 apparatus in the 30–600 °C temperature range at 5 °C/min scan rate and synthetic air flow of 100 mL/min (80 % N_2 + 20 % O_2).

In situ Small Angle X-ray Scattering Kinetics

Methods

In situ Small Angle X-ray Scattering (SAXS) measurements were performed at the BL11 NCD-SWEET beamline from the ALBA Synchrotron Light source (Barcelona, Spain) in terms of the projects ID 2020024318 and 2020094732. Experiments were done using a continuously stirred solution injected into a 2 mm glass capillary's flow cell suitable for liquids in order to ensure a homogeneous nanoparticles distribution during chemical reactions and to diminish the beam damage over the sample. The incoming beam energy was set at 12.4 keV with a sample detector distance of 6700 mm. 2D patterns were recorded in a Pilatus 1 M (Dectris, Switzerland) detector. Each pattern was recorded during 5 seconds with a rate of 4 patterns per minute. The starting cations solution's pH was near 2.5–3 at the beginning of the reaction. Acquisitions started after epoxide dilution into the starting cations solution.

SAXS Models

Samples showed a slope of −2 in *log vs log* scale indicating the formation of 2D objects. To analyze the time-dependent evolution of 2D thin platelets, an interpretation was made using an infinitesimally thin layer model. This model was obtained by factorization of the platelets' thickness (T) and the bidimensional decay at log angles (q^{-2}).[84,85] The polydispersity was fixed at 30 % using a lognormal distribution function (D) centered at the average thickness value T_{av}.

$$P(q, T_{av}) = \frac{1}{q^2}\int_0^{\infty} D(T, T_{av})T^2\left[\frac{\sin(qT/2)}{qT/2}\right]^2 dT \quad (4)$$

The model considered to the scattering intensity ($I(q)$):

$$I(q) = C \cdot P(q,\ T_{av}) + back \quad (5)$$

C, *back* are scalars. Patterns were analysed using an in-house written program in Python 3.8 using the *lmfit* library for least-square procedures.

X-ray Absorption Spectroscopy

X-ray absorption spectroscopy (XAS) measurements were performed at the BL-22 (CLÆSS) beamline from the ALBA synchrotron (Barcelona - Spain). The Co K-edge XANES + EXAFS spectra were measured at room temperature in transmission mode. Absorbents were prepared from fresh powder samples in pellets of 1.3 mm diameter and sealed with Kapton® tape (50 μm in thickness) to prevent the oxidation of the sample. The optimum amount of material for the measurements was calculated by the program hephaestus which is part of the Demeter package.[86] A Si(111) double-crystal monocrhomator was used to obtain a monochromatic incident beam over the sample, and the intensities of incident and transmitted X-rays were measured using two ionization chambers, respectively. EXAFS spectra were collected from 7590–8550 eV with a reduced step (0.3 eV) in the XANES region (7690–7750 eV). The incident photon energy was calibrated using the first inflection point of the Co K-edge (7709 eV) from a reference foil of metallic Co. For each sample three spectra were taken with exposure times of 4 min each one to later be averaged. XANES data treatment was performed by subtracting the pre-edge background followed by normalization by extrapolation of a quadratic polynomial fitted at the post-edge region of the spectrum using ATHENA AUTOBK background removal algorithm.[87] The quantitative analysis of the EXAFS results, were performed by modeling and fitting the insolated EXAFS oscillations. The EXAFS oscillations χ(k) were extracted from the experimental data with standard procedures using the Athena program. k^2 weighted χ(k) data, to enhance the oscillations at higher k, were Fourier transformed. The Fourier transformation was calculated using the sine filtering function. EXAFS modeling was carried out using the ARTEMIS software.[86] Theoretical scattering path amplitudes and phase shifts for all paths used in the fits were calculated using the FEFF9 code.[88] The k-range was set from 2.5–12.8 $Å^{-1}$. The passive reduction factor S_0^2 value was restrained to 0.8. This value was obtained from the fitting of metallic Co foil standard and constraining the coordination numbers to those corresponding to the structure.

DFT + U Calculations

All calculations were performed employing DFT as implemented in the Quantum Espresso code,[89] which is based on the pseudopotential approximation to represent the ion-electron interactions, and plane wave basis sets to expand the Kohn-Sham orbitals. Ultrasoft-type pseudopotentials were adopted, in combination with the Perdew, Burke, and Ernzerhof (PBE) formalism to compute the exchange-correlation term.[90]

According to previous optimizations of related phases, the Hubbard parameter in the DFT + U calculations was fixed at 4.5 eV.[34,38,91–96]

An energy threshold of 10^{-8} au was used for self-consistency, whereas for geometry optimizations, the convergence criteria were 10^{-6} au for the energy and 10^{-3} au for the forces per atom. To improve the numerical convergence, a first-order Methfessel-Paxton spread was implemented. The dispersive interactions were considered by including the DFT + D semiempirical correction originally introduced by Grimme[97] and implemented in a plane wave framework by Barone and co-workers.[98] Noncollinear calculations with spin-orbit contributions[99] were performed to assess the spin orientation of cobalt ions. In our previous study, we found an angle θ = 60° for the magnetic moment of the metal ions with respect to the z axis.[35,38] Thus, unless indicated explicitly, all calculations presented henceforth were performed with this value of θ. The simulations were carried out on supercells with the general formula $[Co_n^{Oh}Co_2^{Td}(OH)_{2n+2}X_2]$, where n = 3, 8 and 15, where the fraction of tetrahedral sites is 0.40, 0.20, and 0.12, respectively and X=Cl, Br and I.[35] These values of n are in line with the chemical compositions observed herein as well as the values reported by other researchers.[36,51,100]

© 2024 The Authors. Batteries & Supercaps published by Wiley-VCH GmbH

25666223, 2024, 11, Downloaded from https://chemistry-europe.onlinelibrary.wiley.com/doi/10.1002/batt.202400335 by University of Ulsan, Wiley Online Library on [11/11/2025]. See the Terms and Conditions (https://onlinelibrary.wiley.com/terms-and-conditions) on Wiley Online Library for rules of use; OA articles are governed by the applicable Creative Commons License

Electrode Preparation

For the electrochemical measurements, firstly a mixture of the LHs, acetylene black and PTFE in ethanol in a mass ratio of 80:10:10 was prepared and deposited on a nickel foam electrode. The as-prepared electrode was let dry for 2 h at 80 °C. Each working electrode contained around 0.8–1.0 mg of LHs sample and a square-like shape with edges of 1 cm.

Electrochemical Characterization

The electrochemical measurements were carried in a typical three-electrode cell equipped with as-prepared deposited Ni foam, stainless steel sheet, and a Metrohm Ag/AgCl (3 M KCl) as working, counter and reference electrode, respectively, while as the electrolyte 6 M KOH (99.99 %) aqueous solutions were employed. All the electrochemical experiments were performed at room temperature using a Gamry Interface 1000 E potentiostat/galvanostat controlled by Gamry's Global Software. Cyclic voltammetry curves (CVs) were carried out in the range from −0.6–0.4 V versus Ag/AgCl at different scan rates (100, 50, 20, 10 and 5 mV/s). Charge/discharge curves were performed in the range −0.1–0.4 V versus Ag/AgCl at different current density (30, 20, 10, 5, 2 and 1 A/g). The measurements were performed at least three times for every sample using different electrodes. The specific capacitance (C) was calculated from the discharge curves according to the following equation:

$$\boldsymbol{C} = (\boldsymbol{i} \cdot \Delta \boldsymbol{t})/(\boldsymbol{m} \cdot \Delta \boldsymbol{V})$$

Where $\boldsymbol{i}$ is the discharge current, $\Delta \boldsymbol{t}$ is the time for a full discharge, $\boldsymbol{m}$ the weight in grams of the LHs material in the electrode layer, and $\Delta \boldsymbol{V}$ is the voltage change after a full discharge. Capacity retention was evaluated during 10000 charge/discharge cycles at a constant current density of 20 A/g. Electrochemical impedance spectroscopy (EIS) measurements were carried out by applying an AC amplitude of 10 mV in the frequency range of 10^{-2}–10^{4} Hz at the open circuit potential. EIS data were analysed and fitted by means of Gamry Echem Analyst v. 7.07 software.

Acknowledgements

This work was supported by the European Research Council (ERC Starting Grant No. 2D- PnictoChem 804110, and ERC Proof of Concept Grant 2D4H2 No. 101101079), the Spanish MCIN/AEI (PID2022-143297NB–I00, TED2021-131347B–I00 and Unit of Excellence "Maria de Maeztu" CEX2019-000919-M), the Generalitat Valenciana (CIDEGENT/2018/001). The authors thank CELLS ALBA (Spain) for providing access to all necessary facilities for conducting the synchrotron radiation experiments under project numbers 2020024318 and 2020094732 (BL11 NCD-SWEET), as well as 2021095464 (BL22-CLÆSS). ASD thanks the Universidad de Valencia for an 'Atracció de talent' predoctoral grant. MM is a research member from CONICET (Argentina) and thanks to the financial support of the institution, from the Agencia Nacional de Promoción Científica y Tecnológica (ANPCyT, PICT2021-I–A-00903), and from the MinCyT through the project RX-EE-1. The authors thank Christian Olivares-Martínez and Juan Munafo Horta for their assistance in the design of the graphic cover. VO thanks ALN for permanent support.

Conflict of Interests

The authors declare no conflict of interest.

Data Availability Statement

The data that support the findings of this study are available from the corresponding author upon reasonable request.

Keywords: 2D materials · Layered materials · Layered hydroxides · Energy storage · Supercapacitors

[1] A. K. Geim, K. S. Novoselov, *Nanosci. Technol.* **2007**, *6*, 9.
[2] F. Bonaccorso, L. Colombo, G. Yu, M. Stoller, V. Tozzini, A. C. Ferrari, R. S. Ruoff, V. Pellegrini, *Science* **2015**, *347*, 1246501.
[3] M. Gibertini, M. Koperski, A. F. Morpurgo, K. S. Novoselov, *Nat. Nanotechnol.* **2019**, *14*, 408–419.
[4] P. Vishnoi, K. Pramoda, C. N. R. Rao, *ChemNanoMat* **2019**, *5*, 1062–1091.
[5] J. Sturala, Z. Sofer, M. Pumera, *Angew. Chem. Int. Ed.* **2019**, *58*, 7551–7557.
[6] J. A. Carrasco, P. Congost-Escoin, M. Assebban, G. Abellán, *Chem. Soc. Rev.* **2023**, *52*, 1288–1330.
[7] X. Kong, Q. Liu, C. Zhang, Z. Peng, Q. Chen, *Chem. Soc. Rev.* **2017**, *46*, 2127–2157.
[8] M. A. Lucherelli, V. Oestreicher, M. Alcaraz, G. Abellán, *Chem. Commun.* **2023**, *59*, 6453–6474.
[9] S. Manzeli, D. Ovchinnikov, D. Pasquier, O. V. Yazyev, A. Kis, *Nat. Rev. Mater.* **2017**, *2*, 1–15.
[10] C. Lan, Z. Zhou, R. Wei, J. C. Ho, *Mater. Today Energy* **2019**, *11*, 61–82.
[11] X. Li, D. Du, Y. Zhang, W. Xing, Q. Xue, Z. Yan, *J. Mater. Chem. A* **2017**, *5*, 15460–15485.
[12] V. Oestreicher, M. Jobbágy, *Langmuir* **2013**, *29*, 12104–12109.
[13] H. Yi, S. Liu, C. Lai, G. Zeng, M. Li, X. Liu, B. Li, X. Huo, L. Qin, L. Li, M. Zhang, Y. Fu, Z. An, L. Chen, *Adv. Energy Mater.* **2021**, *11*, 2002863.
[14] N. Arencibia, V. Oestreicher, F. A. Viva, M. Jobbágy, *RSC Adv.* **2017**, *7*, 5595–5600.
[15] G. Rogez, C. Massobrio, P. Rabu, M. Drillon, *Chem. Soc. Rev.* **2011**, *40*, 1031.
[16] G. Abellán, C. Martí-Gastaldo, A. Ribera, E. Coronado, *Acc. Chem. Res.* **2015**, *48*, 1601–1611.
[17] Z. Cai, X. Bu, P. Wang, J. C. Ho, J. Yang, X. Wang, *J. Mater. Chem. A* **2019**, *7*, 5069–5089.
[18] A. Gomes, D. Cocke, D. Tran, A. Baksi, in *Energy Technology 2015: Carbon Dioxide Management and Other Technologies* (Eds: A. Jha, C. Wang, N. R. Neelameggham, D. P. Guillen, L. Li, C. K. Belt, R. Kirchain, J. S. Spangenberger, F. Johnson, A. J. Gomes, A. Pandey, P. Hosemann), Springer International Publishing, Cham **2016**, 309–316.
[19] M. Gong, Y. Li, H. Wang, Y. Liang, J. Z. Wu, J. Zhou, J. Wang, T. Regier, F. Wei, H. Dai, *J. Am. Chem. Soc.* **2013**, *135*, 8452–8455.
[20] G. Abellán, E. Coronado, C. Martí-Gastaldo, A. Ribera, J. L. Jordá, H. García, *Adv. Mater.* **2014**, *26*, 4156–4162.
[21] J. A. Carrasco, G. Abellán, E. Coronado, *J. Mater. Chem. C* **2018**, *6*, 1187–1198.
[22] A. Seijas-Da Silva, R. Sanchis-Gual, J. A. Carrasco, V. Oestreicher, G. Abellán, E. Coronado, *Batter. Supercaps* **2020**, *3*, 499–509.
[23] J. A. Carrasco, V. Oestreicher, A. S.-D. Silva, G. Abellán, *Appl. Clay Sci.* **2023**, *243*, 107073.
[24] R. Tian, S.-H. Park, P. J. King, G. Cunningham, J. Coelho, V. Nicolosi, J. N. Coleman, *Nat. Commun.* **2019**, *10*, 1933.
[25] J. Yan, Z. Fan, W. Sun, G. Ning, T. Wei, Q. Zhang, R. Zhang, L. Zhi, F. Wei, *Adv. Funct. Mater.* **2012**, *22*, 2632–2641.
[26] J. Xu, S. Gai, F. He, N. Niu, P. Gao, Y. Chen, P. Yang, *Dalton Trans.* **2014**, *43*, 11667–11675.
[27] P. Xiong, X. Zhang, H. Wan, S. Wang, Y. Zhao, J. Zhang, D. Zhou, W. Gao, R. Ma, T. Sasaki, G. Wang, *Nano Lett.* **2019**, *19*, 4518–4526.
[28] K. Le, Z. Wang, F. Wang, Q. Wang, Q. Shao, V. Murugadoss, S. Wu, W. Liu, J. Liu, Q. Gao, Z. Guo, *Dalton Trans.* **2019**, *48*, 5193–5202.
[29] G. Abellán, J. A. Carrasco, E. Coronado, in *Layered Double Hydroxide Polymer Nanocomposites:* Layered double hydroxide nanocomposites

© 2024 The Authors. Batteries & Supercaps published by Wiley-VCH GmbH

25666223, 2024, 11, Downloaded from https://chemistry-europe.onlinelibrary.wiley.com/doi/10.1002/batt.202400335 by University of Ulsan, Wiley Online Library on [11/11/2025]. See the Terms and Conditions (https://onlinelibrary.wiley.com/terms-and-conditions) on Wiley Online Library for rules of use; OA articles are governed by the applicable Creative Commons License

based on carbon nanoforms, (Eds: S. Thomas, S.Daniel), Woodhead Publishing, Elsevier **2020**, 411–460.
[30] K. Li, C. Yin, X. Dai, J. Zhang, S. Yi, J. Rao, Y. Zhang, *J. Storage Mater.* **2022**, *55*, 105722.
[31] P. Li, X. Duan, Y. Kuang, Y. Li, G. Zhang, W. Liu, X. Sun, *Adv. Energy Mater.* **2018**, *8*, 1703341.
[32] A. Tyagi, M. Chandra Joshi, K. Agarwal, B. Balasubramaniam, R. K. Gupta, *Nanoscale Adv.* **2019**, *1*, 2400–2407.
[33] L. Zhou, C. Zhang, Y. Zhang, Z. Li, M. Shao, *Adv. Funct. Mater.* **2021**, *31*, 2009743.
[34] R. Sanchis-Gual, D. Hunt, C. Jaramillo-Hernández, A. Seijas-Da Silva, M. Mizrahi, C. Marini, V. Oestreicher, G. Abellán, *ACS Catal.* **2023**, *13*, 10351–10363.
[35] V. Oestreicher, D. Hunt, R. Torres-Cavanillas, G. Abellán, D. A. Scherlis, M. Jobbágy, *Inorg. Chem.* **2019**, *58*, 9414–9424.
[36] R. Ma, Z. Liu, K. Takada, K. Fukuda, Y. Ebina, Y. Bando, T. Sasaki, *Inorg. Chem.* **2006**, *45*, 3964–3969.
[37] V. Oestreicher, M. Jobbágy, *Chem. Eur. J.* **2019**, *25*, 12611–12619.
[38] D. Hunt, M. Jobbagy, D. A. Scherlis, *Inorg. Chem.* **2018**, *57*, 4989–4996.
[39] R. Tian, M. Breshears, D. V. Horvath, J. N. Coleman, *ACS Nano* **2020**, *14*, 3129–3140.
[40] H. Sun, J. Zhu, D. Baumann, L. Peng, Y. Xu, I. Shakir, Y. Huang, X. Duan, *Nat. Rev. Mater.* **2019**, *4*, 45–60.
[41] H. Xia, Q. Xu, J. Zhang, *Nano-Micro Lett.* **2018**, *10*, 66.
[42] K. Li, H. Teng, X. Dai, Y. Wang, D. Wang, X. Zhang, Y. Yao, X. Liu, L. Feng, J. Rao, Y. Zhang, *CrystEngComm* **2022**, *24*, 2081–2088.
[43] V. Oestreicher, I. Fábregas, M. Jobbágy, *J. Phys. Chem. C* **2014**, *118*, 30274–30281.
[44] P. Borovik, V. Oestreicher, C. Huck-Iriart, M. Jobbágy, *Chem. Eur. J.* **2021**, *27*, 10077–10086.
[45] V. Oestreicher, C. Huck-Iriart, G. Soler-Illia, P. C. Angelomé, M. Jobbágy, *Chem. Eur. J.* **2020**, *26*, 3157–3165.
[46] G. Quintero-Marquina, G. Segovia, V. Oestreicher, D. Lamas, C. Huck-Iriart, ChemRixv **2024**, DOI: 10.26434/chemrxiv-2024-8jqp7
[47] G. M. Segovia, P. Rivas-Rojas, M. Perullini, M. Jobbágy, P. C. Angelomé, C. Huck-Iriart, V. Oestreicher, *J. Phys. Chem. C* **2024**, *128*, 10586–10594.
[48] G. Segovia, C. Huck-Iriart, V. Oestreicher, P. Angelomé, ChemRixv **2024** DOI: 10.26434/chemrxiv-2024-98cpq.
[49] V. Oestreicher, C. Dolle, D. Hunt, M. Fickert, G. Abellán, *Nano Mater. Sci.* **2022**, *4*, 36–43.
[50] Z. Liu, R. Ma, M. Osada, K. Takada, T. Sasaki, *J. Am. Chem. Soc.* **2005**, *127*, 13869–13874.
[51] J. R. Neilson, J. A. Kurzman, R. Seshadri, D. E. Morse, *Chem. Eur. J.* **2010**, *16*, 9998–10006.
[52] D. Hunt, V. Oestreicher, M. Mizrahi, F. G. Requejo, M. Jobbágy, *Chem. Eur. J.* **2020**, *26*, 17081–17090.
[53] V. Oestreicher, D. Hunt, C. Dolle, P. Borovik, M. Jobbágy, G. Abellán, E. Coronado, *Chem. Eur. J.* **2021**, *27*, 921–927.
[54] J. R. Neilson, B. Schwenzer, R. Seshadri, D. E. Morse, *Inorg. Chem.* **2009**, *48*, 11017–11023.
[55] J. Lewis, *Sci. Pro. (1933–)* **1963**, *51*, 450–473.
[56] V. Oestreicher, G. Abellán, E. Coronado, *Phys. Rapid Res. Ltrs.* **2020**, *14*, 2000380.
[57] M. C. Biesinger, B. P. Payne, A. P. Grosvenor, L. W. M. Lau, A. R. Gerson, R. St, *Appl. Surf. Sci.* **2011**, *257*, 2717–2730.
[58] P. Simon, Y. Gogotsi, *Nat. Mater.* **2008**, *7*, 845–854.
[59] T. M. Masikhwa, M. J. Madito, D. Y. Momodu, J. K. Dangbegnon, O. Guellati, A. Harat, M. Guerioune, F. Barzegar, N. Manyala, *RSC Adv.* **2016**, *6*, 46723–46732.
[60] A. D. Jagadale, V. S. Kumbhar, D. S. Dhawale, C. D. Lokhande, *Electrochim. Acta* **2013**, *98*, 32–38.
[61] A. Seijas-Da Silva, V. Oestreicher, E. Coronado, G. Abellán, *Dalton Trans.* **2022**, *51*, 4675–4684.
[62] J. A. Carrasco, R. Sanchis-Gual, A. S.-D. Silva, G. Abellán, E. Coronado, *Chem. Mater.* **2019**, *31*, 6798–6807.
[63] X. Gao, X. Liu, D. Wu, B. Qian, Z. Kou, Z. Pan, Y. Pang, L. Miao, J. Wang, *Adv. Funct. Mater.* **2019**, *29*, 1903879.
[64] Y. Wang, W. Yang, C. Chen, D. G. Evans, *J. Power Sources* **2008**, *184*, 682–690.
[65] E. Boccalon, G. Gorrasi, M. Nocchetti, *Adv. Colloid Interface Sci.* **2020**, *285*, 102284.
[66] L.-J. Zhou, X. Huang, H. Chen, P. Jin, G.-D. Li, X. Zou, *Dalton Trans.* **2015**, *44*, 11592–11600.
[67] T. Dong, X. Zhang, M. Li, P. Wang, P. Yang, *Inorg. Chem. Front.* **2018**, *5*, 3033–3041.
[68] C. Jing, B. Dong, Y. Zhang, *Energy Environ. Mater.* **2020**, *3*, 346–379.
[69] Z.-A. Hu, Y.-L. Xie, Y.-X. Wang, L.-J. Xie, G.-R. Fu, X.-Q. Jin, Z.-Y. Zhang, Y.-Y. Yang, H.-Y. Wu, *J. Phys. Chem. C* **2009**, *113*, 12502–12508.
[70] L. Wang, Z. H. Dong, Z. G. Wang, F. X. Zhang, J. Jin, *Adv. Funct. Mater.* **2013**, *23*, 2758–2764.
[71] X. Liu, R. Ma, Y. Bando, T. Sasaki, *Adv. Mater.* **2012**, *24*, 2148–2153.
[72] L. Liu, J. P. Cheng, J. Zhang, F. Liu, X. B. Zhang, *J. Alloys Compd.* **2014**, *615*, 868–874.
[73] K. Li, H. Teng, Q. Sun, Y. Li, X. Wu, X. Dai, Y. Wang, S. Wang, Y. Zhang, K. Yao, Z. Bao, J. Rao, Y. Zhang, *J. Storage Mater.* **2022**, *53*, 105094.
[74] B. K. Lesel, J. S. Ko, B. Dunn, S. H. Tolbert, *ACS Nano* **2016**, *10*, 7572–7581.
[75] V. Augustyn, P. Simon, B. Dunn, *Energy Environ. Sci.* **2014**, *7*, 1597.
[76] D. Chao, C. Zhu, P. Yang, X. Xia, J. Liu, J. Wang, X. Fan, S. V. Savilov, J. Lin, H. J. Fan, Z. X. Shen, *Nat. Commun.* **2016**, *7*, 12122.
[77] S. Fleischmann, J. B. Mitchell, R. Wang, C. Zhan, D. Jiang, V. Presser, V. Augustyn, *Chem. Rev.* **2020**, *120*, 6738–6782.
[78] J. Zhang, X. Wang, J. Ma, S. Liu, X. Yi, *Electrochim. Acta* **2013**, *104*, 110–116.
[79] G. Zhang, J. Hu, Y. Nie, Y. Zhao, L. Wang, Y. Li, H. Liu, L. Tang, X. Zhang, D. Li, L. Sun, H. Duan, *Adv. Funct. Mater.* **2021**, *31*, 2100290.
[80] K. Kirshenbaum, D. C. Bock, C.-Y. Lee, Z. Zhong, K. J. Takeuchi, A. C. Marschilok, E. S. Takeuchi, *Science* **2015**, *347*, 149–154.
[81] M. Liang, M. Zhao, H. Wang, J. Shen, X. Song, *J. Mater. Chem. A* **2018**, *6*, 2482–2493.
[82] Q. Jiang, F. Liu, T. Li, T. Xu, *J. Mater. Chem. C* **2014**, *2*, 618–621.
[83] Z. Liu, R. Ma, M. Osada, N. Iyi, Y. Ebina, K. Takada, T. Sasaki, *J. Am. Chem. Soc.* **2006**, *128*, 4872–4880.
[84] H. Xing, S. M. Chin, V. R. Udumula, M. Krishnaiah, N. Rodrigues De Almeida, C. Huck-Iriart, A. S. Picco, S. R. Lee, G. Zaldivar, K. A. Jackson, M. Tagliazucchi, S. I. Stupp, M. Conda-Sheridan, *Biomacromolecules* **2021**, *22*, 3274–3283.
[85] G. Porod, *Acta Phys. Austriaca* **1948**, *2*, 255–292.
[86] B. Ravel, M. Newville, *J. Synchrotron Rad.* **2005**, *12*, 537–541.
[87] M. Newville, *J. Synchrotron Rad.* **2001**, *8*, 322–324.
[88] J. J. Rehr, J. J. Kas, F. D. Vila, M. P. Prange, K. Jorissen, *Phys. Chem. Chem. Phys.* **2010**, *12*, 5503.
[89] P. Giannozzi, S. Baroni, N. Bonini, M. Calandra, R. Car, C. Cavazzoni, D. Ceresoli, G. L. Chiarotti, M. Cococcioni, I. Dabo, A. Dal Corso, S. De Gironcoli, S. Fabris, G. Fratesi, R. Gebauer, U. Gerstmann, C. Gougoussis, A. Kokalj, M. Lazzeri, L. Martin-Samos, N. Marzari, F. Mauri, R. Mazzarello, S. Paolini, A. Pasquarello, L. Paulatto, C. Sbraccia, S. Scandolo, G. Sclauzero, A. P. Seitsonen, A. Smogunov, P. Umari, R. M. Wentzcovitch, *J. Phys.: Condens. Matter* **2009**, *21*, 395502.
[90] J. P. Perdew, K. Burke, M. Ernzerhof, *Phys. Rev. Lett.* **1997**, *78*, 1396–1396.
[91] J. Chen, A. Selloni, *J. Phys. Chem. C* **2013**, *117*, 20002–20006.
[92] S. Wang, W. Zhao, F. Giustiniano, G. Eda, *Phys. Chem. Chem. Phys.* **2016**, *18*, 4304–4309.
[93] V. I. Anisimov, J. Zaanen, O. K. Andersen, *Phys. Rev. B* **1991**, *44*, 943–954.
[94] L. Wang, T. Maxisch, G. Ceder, *Phys. Rev. B* **2006**, *73*, 195107.
[95] A.-L. Dalverny, J.-S. Filhol, F. Lemoigno, M.-L. Doublet, *J. Phys. Chem. C* **2010**, *114*, 21750–21756.
[96] J. Chen, X. Wu, A. Selloni, *Phys. Rev. B* **2011**, *83*, 245204.
[97] S. Grimme, *J. Comput. Chem.* **2006**, *27*, 1787–1799.
[98] V. Barone, M. Casarin, D. Forrer, M. Pavone, M. Sambi, A. Vittadini, *J. Comput. Chem.* **2009**, *30*, 934–939.
[99] A. D. Corso, A. M. Conte, *Phys. Rev. B* **2005**, *71*, 115106.
[100] Y. Du, D. O'Hare, *Inorg. Chem.* **2008**, *47*, 11839–11846.

Manuscript received: May 20, 2024
Revised manuscript received: July 24, 2024
Accepted manuscript online: July 27, 2024
Version of record online: September 13, 2024

© 2024 The Authors. Batteries & Supercaps published by Wiley-VCH GmbH

25666223, 2024, 11, Downloaded from https://chemistry-europe.onlinelibrary.wiley.com/doi/10.1002/batt.202400335 by University of Ulsan, Wiley Online Library on [11/11/2025]. See the Terms and Conditions (https://onlinelibrary.wiley.com/terms-and-conditions) on Wiley Online Library for rules of use; OA articles are governed by the applicable Creative Commons License